# Electronic Supplementary Information

## Surface Fluorine Preservation-Dependent $Ti_3C_2T_x$ MXene for High Electrochemical Properties in Ionic Liquid Electrolytes

Guangyu Wang,[†,⊥] Hao Wu,[‡,⊥] Yiming Liu,[†] Yiwei Pang,[‡] Junsheng Hao,[†] Fangqin Cheng,[‡] Aniu Qian,[*,‡] and Hu Shi[*,†]

† School of Chemistry and Chemical Engineering, Institute of Molecular Science, Shanxi University, Taiyuan 030006, P. R. China

‡ Institute of Resources and Environment Engineering, Shanxi University, Taiyuan 030006, P. R. China

*KEYWORDS: Surface terminations, MXenes, Terminal substitution mechanism, Electrochemical pseudo-capacitance, Dispersion interactions*

*E-mail: hshi@sxu.edu.cn
*E-mail: anqian@sxu.edu.cn

## EXPERIMENTAL SECTION

**Materials.** $Ti_3AlC_2$ (purity 98%) was purchased from Forsman China. Hydrochloric acid (HCl, 12 M), ethanol (EtOH, 99.98%), dimethylsulfoxide (DMSO, 99.8%), polyvinylidene fluoride (PVDF), and lithium fluoride (LiF, 99.9%) were purchased from Shanghai Macklin Biochemical Co. Ltd. Carbon black (ECP-600JD, Japan) were purchased from Lion specialty chemicals. 1-ethly-3-methylimidazolium bis-(trifluoromethylsulfonyl)-imide (EMITFSI, 98%) and acetonitrile (ACN) were purchased from Sigma Aldrich. Nylon membranes (0.2 μm pore size, German) were purchased from Whatman.

**Preparation of multilayer $Ti_3C_2T_x$.** Multilayer $Ti_3C_2T_x$ was prepared via the *in situ*-formed HF etchants using LiF–HCl solutions. Briefly, 1 g LiF was immersed and stirred for 5 min in 20 mL of 9 M HCl aqueous solution at room temperature. Then 1.5 g $Ti_3AlC_2$ was slowly added to the mixture and stirred at 35°C for 24 h at 1000 rpm. After etching, the mixture was washed several times with DI water and centrifuged at 7000 rpm with 5 min per cycle until the pH reached 6 to achieve dark-green supernatants. The obtained $Ti_3C_2T_x$ sediment was dispersed with DI water, suction-filtrated on the Nylon membrane, dried at room temperature, and stored under vacuum for further use.

**Delamination of multilayer $Ti_3C_2T_x$ nanosheets and its solvent treatment.** Etched $Ti_3C_2T_x$ products (0.2 g) were added to 15 mL DMSO by vigorously stirring for 24 h at room temperature. After delamination, the DMSO-delaminated mixture colloidal solution of $Ti_3C_2T_x$ delamination was subjected to a treatment using the ethanol and DI water, respectively. Through sonication at room temperature for 1 h, the solution was centrifuged for 10 min at 10000 rpm each to separate the delaminated $Ti_3C_2T_x$ sheets from

few-layer $Ti_3C_2T_x$ suspension liquid. Finally, a transparent black EtOH-treated $Ti_3C_2T_x$ suspension and a thick dark-green DI-treated $Ti_3C_2T_x$ suspension were obtained separately. For experimental dispersion behaviors, the dispersions were performed by pipetting 1 mL of the $Ti_3C_2T_x$ suspension into 20 mL vial with each solvent. The DI-treated and EtOH-treated $Ti_3C_2T_x$ are suspended in DI and EtOH solvents, respectively.

**Materials characterizations**. The $Ti_3C_2T_x$ morphology was observed by using SEM (JEOL, JSM-IT500HR) and AFM (Bruker Dimension Icon, Multimode 8). The phase structure of $Ti_3C_2T_x$ was characterized using XRD (Bruker AXS) with a Cu Kα (λ = 1.54 Å) radiation at 40 kV and 40 mA and a $2\theta$ = 5-80° at 0.175°$s^{-1}$, of which a smooth polyethylene terephthalate (PET, Sigma Aldrich) substrate was used for XRD. The particle size distribution was collected using laser particle size analyzer (Malvern-MAZ 3000, UK). Attenuated total reflectance Fourier transform infrared spectroscopy (ATR-FTIR, Thermo Fisher Scientific Nicolet iS50R) measurements were conducted at a wavenumber range of 400 to 4000 $cm^{-1}$ on an indium tin oxide (ITO) glass substrate. The peak intensity ratio of $I_{C-F\ bond}/I_{C-F\ bond}$ and $I_{C-O\ bond}/I_{C-O\ bond}$ for EtOH- and DI-treated $Ti_3C_2T_x$ are 0.16 and 0.13, respectively. Surface terminal group was obtained by X-ray photoelectron spectroscopy (XPS, Thermo Kalpha) with an $AlK_\alpha$ source (hν = 1486.6 eV). UV-visible absorbance spectroscopy (10 mm optical path length cell, HITACHI, UH5700) was scanned at a wavelength range of 200 to 1000 $nm^{-1}$.

**Electrochemical measurements.** Cyclic Voltammetry (CV), Galvanostatic charge-discharge (GCD), and electrochemical impedance spectroscopy (EIS) measurements were performed on a CHI 660E electrochemical workstation, where a three-electrode

Swagelok© configuration in acetonitrile-dissolved 1 M EMITFSI ionic liquid as electrolytes comprised a Pt plate, Ag wire, and $Ti_3C_2T_x$ as the counter, reference, and working electrodes, respectively. The pseudo-capacitors were assembled in argon-atmosphere glove box. The working electrode was fabricated by spraying and drying a homogeneous slurry onto a glass-carbon current collector at 80°C, where the slurry dissolves DI-treated and EtOH-treated $Ti_3C_2T_x$ delamination solutions, PVDF, and conductive carbon black with a weight ratio of 80:10:10 in diluted ethanol solution. For comparison, 2 M KCl aqueous electrolytes in a three-electrode configuration were assembled, in which a Pt plate, Ag/AgCl, and $Ti_3C_2T_x$ as the counter, reference, and working electrodes, respectively. The working electrode was fabricated by dip-coating DI- and EtOH-treated $Ti_3C_2T_x$ delamination solutions in the high-conductivity and low-electrochemical-interference ITO glass substrate. CV was conducted by using a scan rate ranged from 5 mV $s^{-1}$ to 1000 mV $s^{-1}$. EIS data was collected with a 5 mV amplitude at a frequency ranged from 10 mHz to 100 kHZ. Mass loadings of DI- and EtOH-treated $Ti_3C_2T_x$ electrodes were 1 mg, respectively. The gravimetric capacitance ($C_g$, F $g^{-1}$) was calculated using the formula:

$$C_g = \frac{1}{\nu m \Delta V} \int i dV$$

where $\nu$ is the scan rate (mV $s^{-1}$), $i$ is the current density (A $g^{-1}$), ΔV is the potential window (V), and m is mass loadings.

**Simulation Methods**

Considering the different functional groups coexisted in $Ti_3C_2T_x$ surface, we used a same mixture $Ti_3C_2T_x$ structure as the initial structure (including $-CF_3$, –F, –O, –OH) for two

MD systems ($Ti_3C_2T_x$+DI and $Ti_3C_2T_x$+EtOH). To obtain the optimized initial structure of $Ti_3C_2T_x$ MXene system, density functional theory (DFT) calculations were performed using the Vienna *Ab Initio* Simulation Package (VASP)[1] with generalized gradient approximation (GGA) and the projector-augmented wave (PAW) method. Lattice parameters are *a*=1.2 nm, *b*=1.2 nm, *c*=3.0 nm, α=β=90.00°, and γ=120.00°. The standard precision was selected. The kinetic energy cutoff was set at 400 eV. After the DFT optimization (Figure S11), we expanded into 3×3 supercell along *a* and *b* axis for further calculation modelling. Classical molecular dynamic (MD) simulations were performed to investigate the different phenomena under DMSO with water or EtOH molecules. Here, the simulation parameters of $Ti_3C_2T_x$ was obtained using UFF force filed[2] which has been confirmed the accuracy in literatures[3]. The simulation parameters of DMSO and EtOH were generated by Amber 18[4] and Gaussian 09 software[5] at the B3LYP/6-31G* level. Additionally, the force field of water was obtained using the TIP3P parameters. During MD simulations, the Particle-mesh Ewald was selected for long-range electrostatics, the cutoff was set at 0.8 nm, and the time step was set at 1 fs. In water system, it contains 169 DMSO molecules and 1333 water molecules at the size of *a*=3.7 nm, *b*=3.7 nm, *c*=5.7 nm, α=β=90.00°, and γ=120.00°. In EtOH system, it contains 110 DMSO molecules and 269 EtOH molecules at the size of *a*=3.7 nm, *b*=3.7 nm, *c*=5.1 nm, α=β=90.00°, and γ=120.00°. Finally, 300 ns MD simulations were performed for each system; after equilibration checking, only the final 50 ns converging trajectory was used for further analysis.

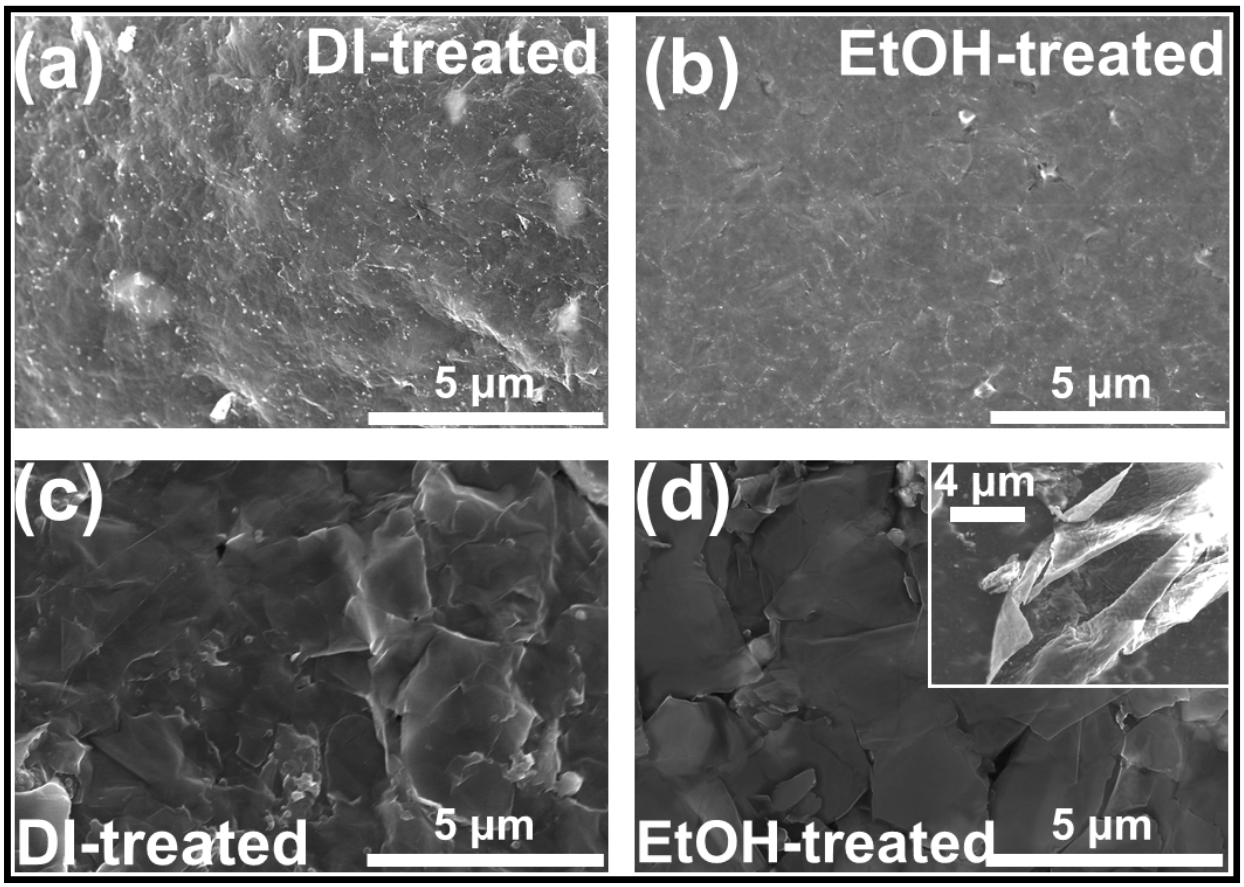


Figure S1. SEM images of DI-treated and EtOH-treated multilayered $Ti_3C_2T_x$ MXene flakes in (a–b) high and (c–d) low concentrations, respectively.

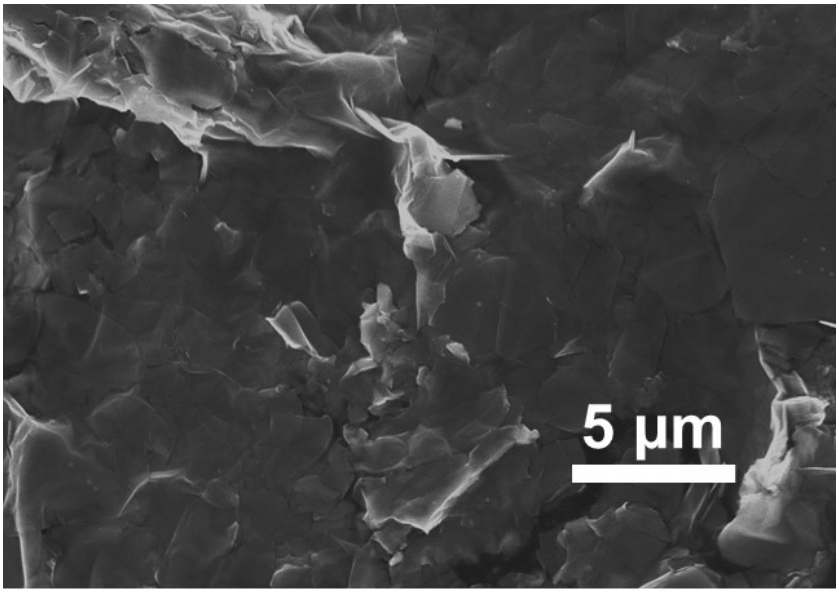


Figure S2. SEM images of the delaminated $Ti_3C_2T_x$ flakes before the treatments of DI and EtOH solvent.

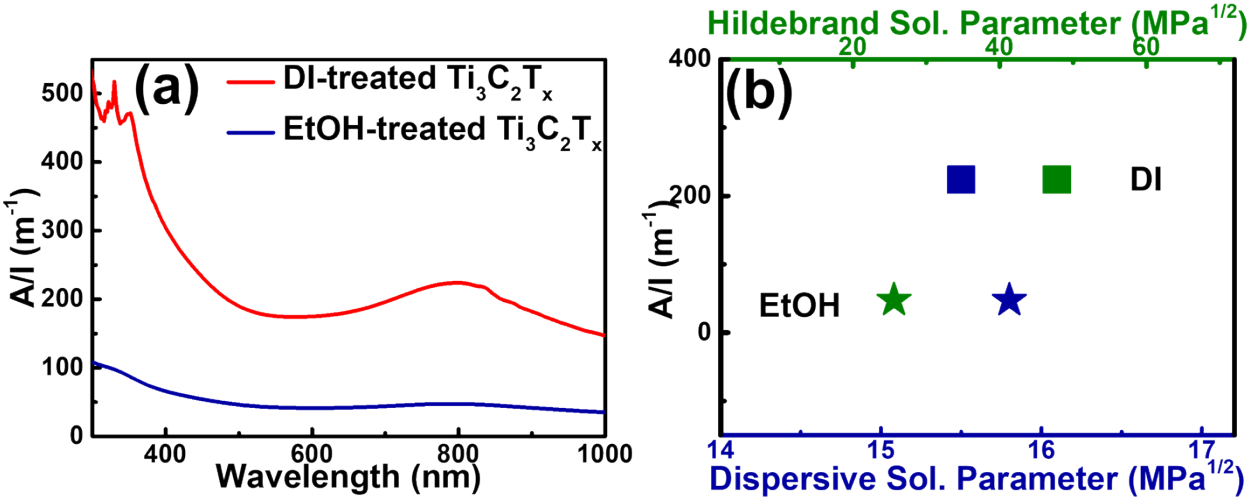


Figure S3. (a) UV-visible absorbance spectra, (b) Hildebrand solubility parameters and dispersive associated Hansen solubility parameters with respect to solvent-treated $Ti_3C_2T_x$ absorbance per cell path length ($A/l$) at 800 nm.

**Table S1** Hansen solubility parameters and Hildebrand solubility parameters of EtOH and DI water in this study

| Solvent | Hansen and Hildebrand solubility parameters | | | | |
|---|---|---|---|---|---|
| | Polar ($MPa^{1/2}$) | Dispersive ($MPa^{1/2}$) | H-bonding ($MPa^{1/2}$) | Hildebrand ($MPa^{1/2}$) | $A/l$ ($m^{-1}$) |
| Ethanol | 9 | 15.7 | 19 | 26 | 47.5 |
| DI water | 16 | 15.4 | 41 | 49 | 224 |

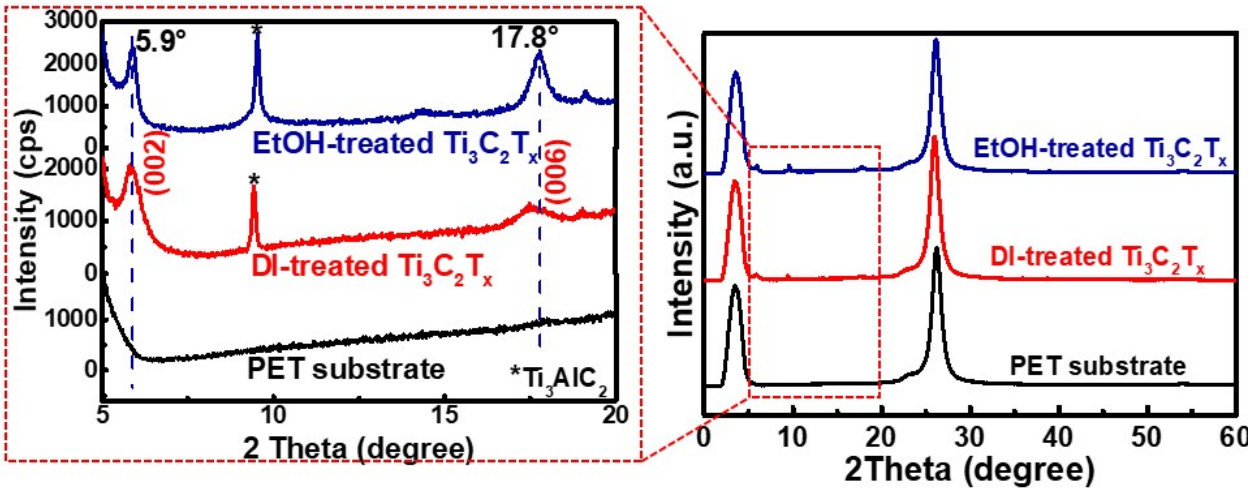


Figure S4. XRD patterns of EtOH-treated and DI-treated $Ti_3C_2T_x$.

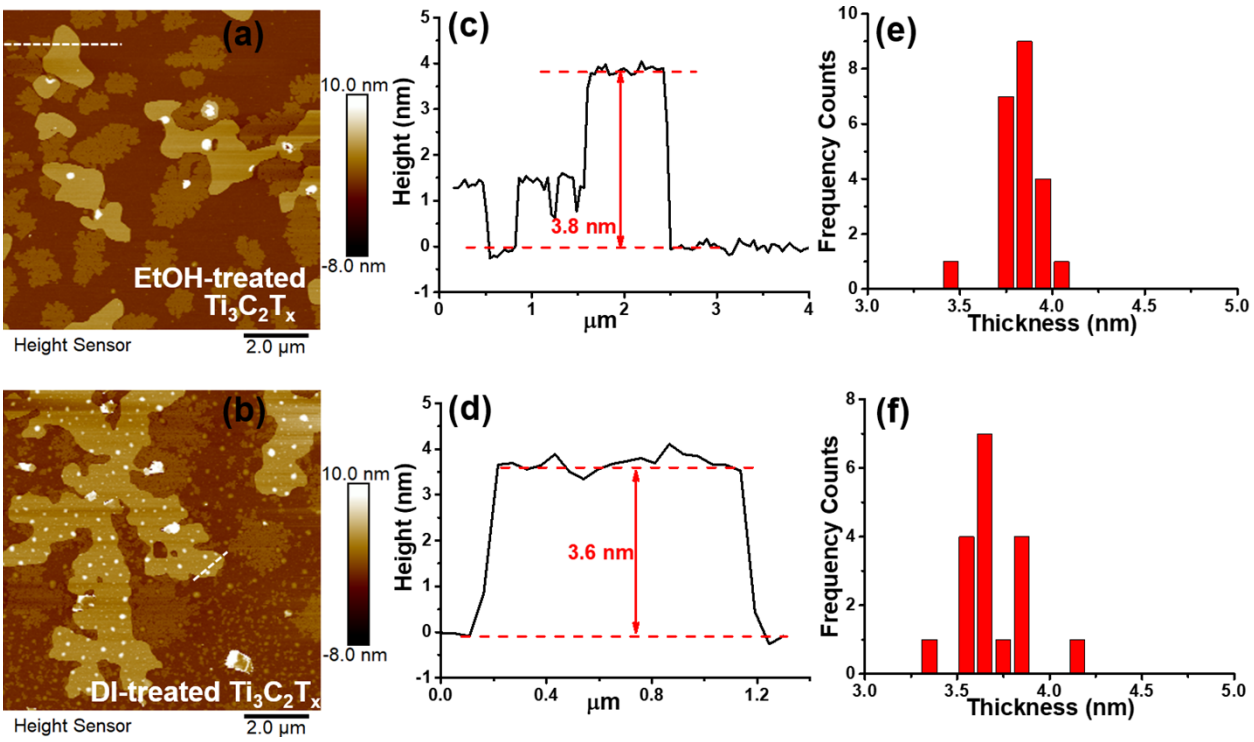


Figure S5. (a, b) AFM images, (c, d) corresponding height profile, and (e, f) statistical thickness distribution of EtOH-treated and DI-treated $Ti_3C_2T_x$.

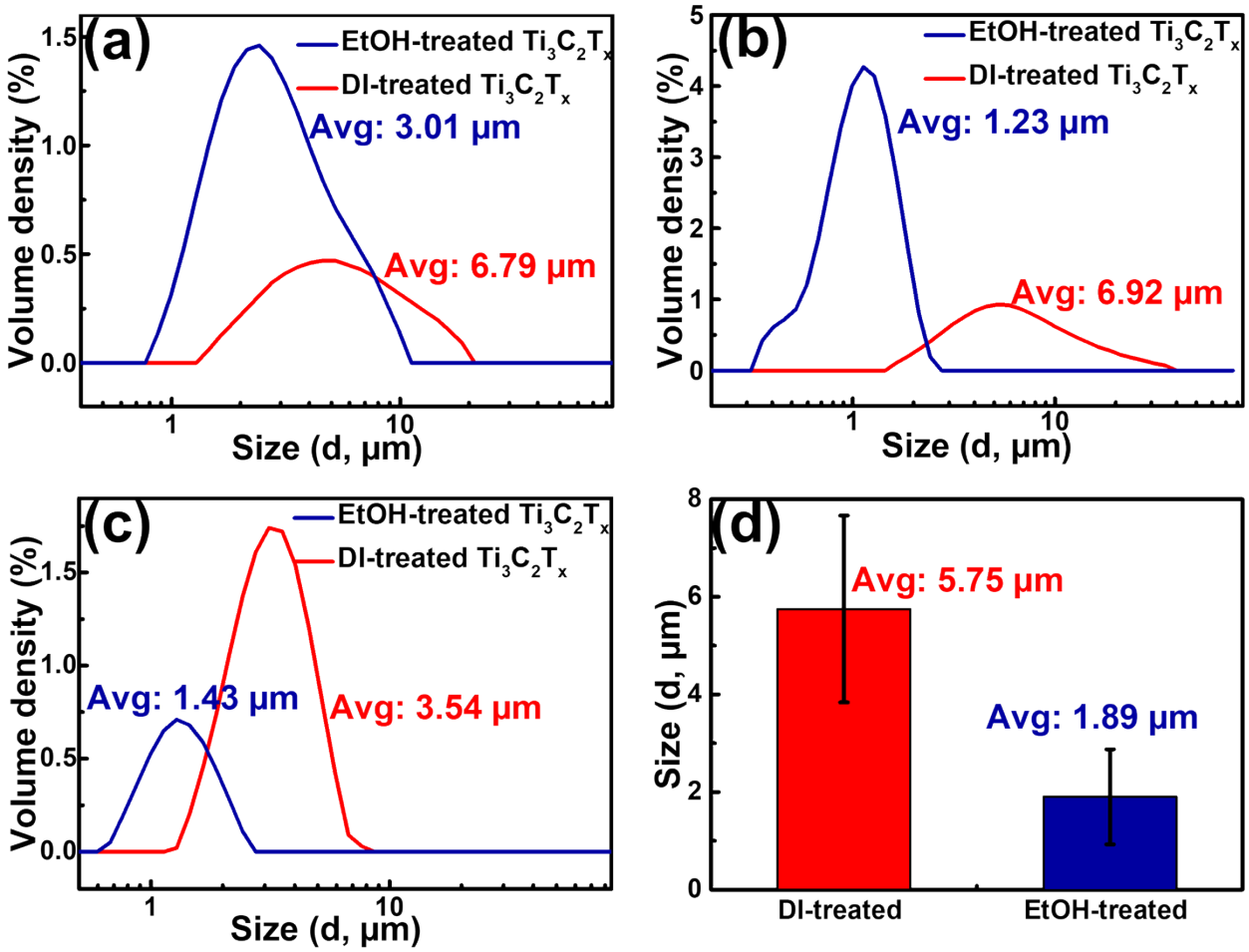


Figure S6. Supplementary experimental-measured size distributions (a-c) of EtOH-treated and DI-treated $Ti_3C_2T_x$ delamination suspension, and their corresponding vertical error bars (d) in the size data.

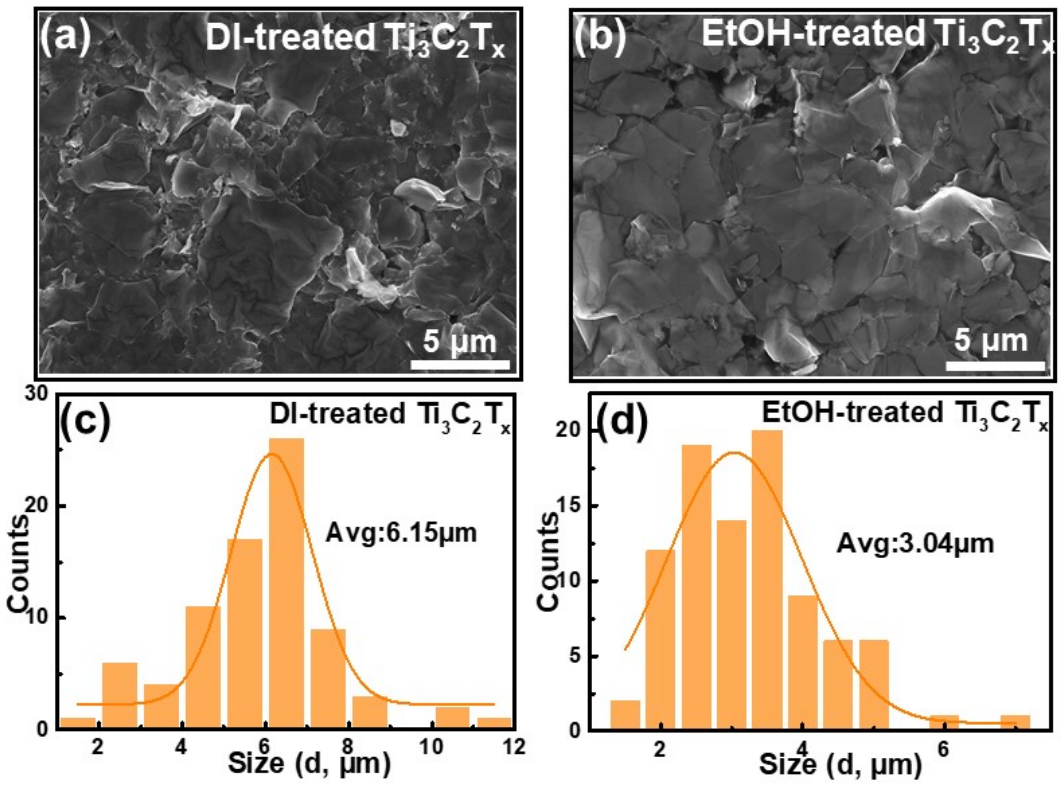


Figure S7. (a, b) SEM images and corresponding (c, d) size distribution of EtOH-treated and DI-treated $Ti_3C_2T_x$.

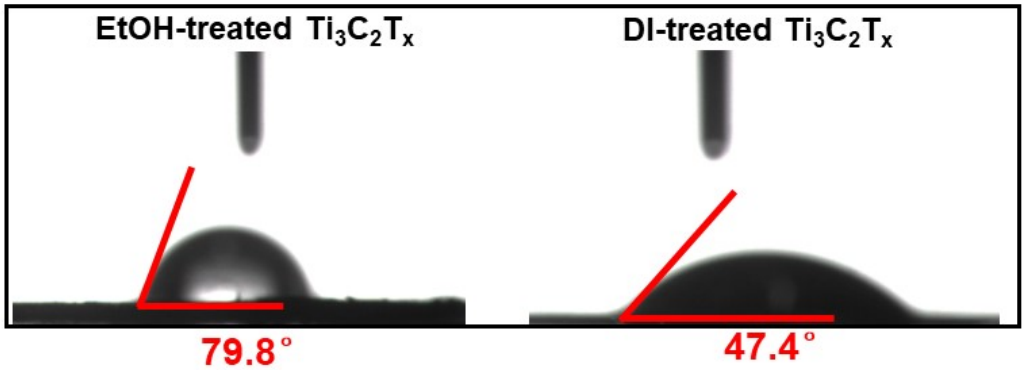


Figure S8. Contact angle of DI-treated and EtOH-treated $Ti_3C_2T_x$.

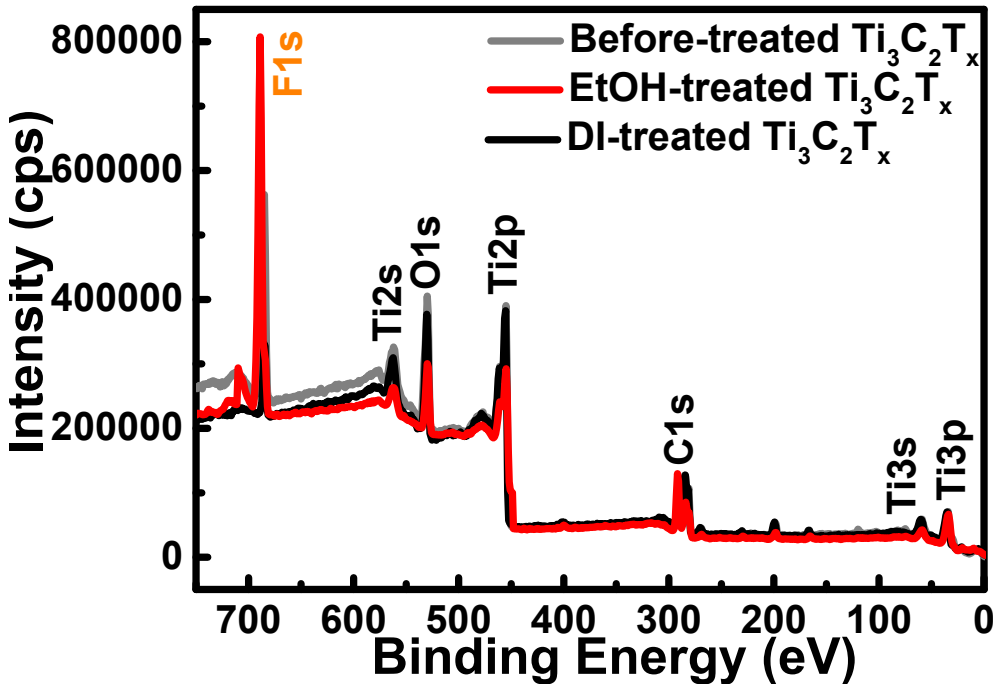


Figure S9. XPS of EtOH-treated, DI-treated, and solvent-free treated $Ti_3C_2T_x$.

**Table S2** XPS peak fitting of EtOH-treated and DI-treated $Ti_3C_2T_x$

| Element info. | Description | Binding Energy (eV) | | | | | | | |
|---|---|---|---|---|---|---|---|---|---|
| $Ti_{2p}$ | EtOH-treated | 454.6 | 455.7 | 458.7 | 460.6 | 461.7 | 463.2 | 464.4 | 456.9 |
| | DI-treated | 454.3 | 455.4 | 458.5 | 460.3 | 461.3 | 462.4 | 464.1 | 456.6 |
| | Assigned to | Ti-C 2p3/2 | Ti(II) 2p3/2 | Ti-O 2p3/2 | Ti-C 2p1/2 | Ti(II) 2p1/2 | Ti-C 2p1/2 | Ti-O 2p1/2 | $Ti_xO_y$ |
| | Reference | 6 | 7 | 8 | 9 | 10 | 10 | 6 | 11 |
| C 1s | EtOH-treated | 281.3 | 282.3 | 284.4 | 286.0 | 287.3 | 288.6 | 290.5 | 292.0 |
| | DI-treated | 281.1 | 282.0 | 283.8 | 285.7 | 287.3 | 288.4 | - | - |
| | Assigned to | C-Ti | C-Ti-O | C-C | C-O | OH-C=O | O-C=O, C-F | $CF_2$ | $CF_3$ |
| | Reference | 11 | 12 | 13 | 13 | 14 | 11 | 15 | 15 |
| O 1s | EtOH-treated | 529.4 | 530.6 | 531.9 | 533.1 | | | | |
| | DI-treated | 529.1 | 530.2 | 531.5 | 532.7 | | | | |
| | Assigned to | O-Ti | C-Ti-$O_x$ | C-Ti-$(OH)_x$ | C-Ti-$(OH)_x$-$H_2O$ | | | | |
| | Reference | 7 | 10 | 10 | 12 | | | | |
| F 1s | EtOH-treated | 684.6 | 685.6 | 689.3 | | | | | |
| | DI-treated | 684.3 | 685.7 | 688.1 | | | | | |
| | Assigned to | F-Ti | F-Al | F-C | | | | | |
| | Reference | 16 | 17 | 15 | | | | | |

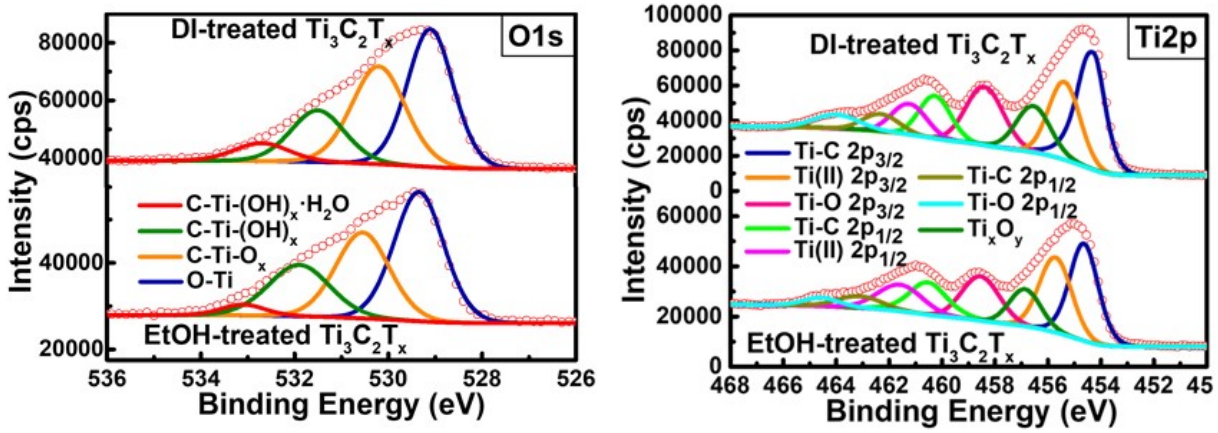


Figure S10. High-resolution XPS of O 1s and Ti 2p core levels for EtOH-treated and DI-treated $Ti_3C_2T_x$.

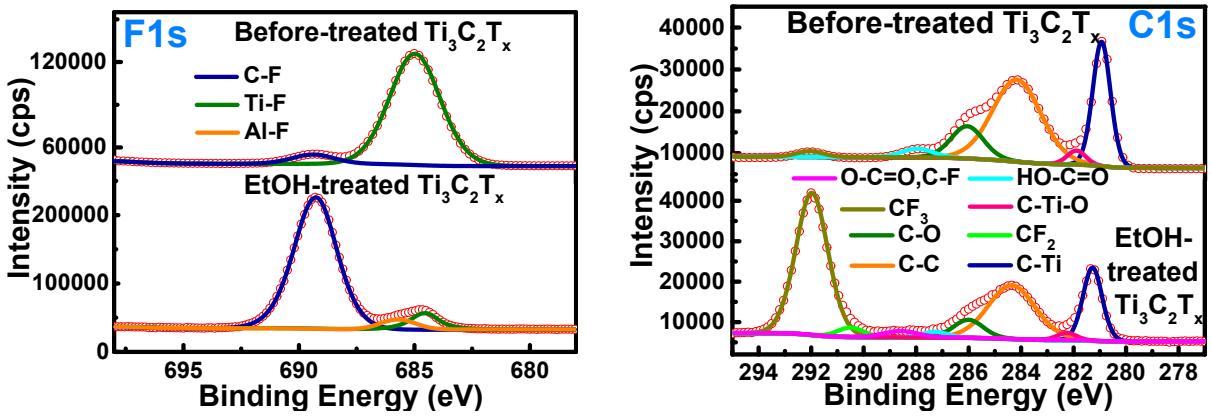


Figure S11. High-resolution XPS of F 1s and C 1s core levels for EtOH-treated and solvent-free treated $Ti_3C_2T_x$.

**Table S3** XPS data of the EtOH- and DI-treated $Ti_3C_2T_x$

| XPS content (at%) | Elements containing | | | | |
|---|---|---|---|---|---|
| | C | Ti | O | F | Ti/C |
| Solvent free-treated $Ti_3C_2T_x$ | 33.45 | 20.74 | 23.25 | 22.56 | 0.62 |
| EtOH-treated $Ti_3C_2T_x$ | 18.54 | 13.05 | 12.47 | 55.94 | 0.70 |
| DI-treated $Ti_3C_2T_x$ | 40.49 | 26.25 | 23.53 | 9.73 | 0.65 |

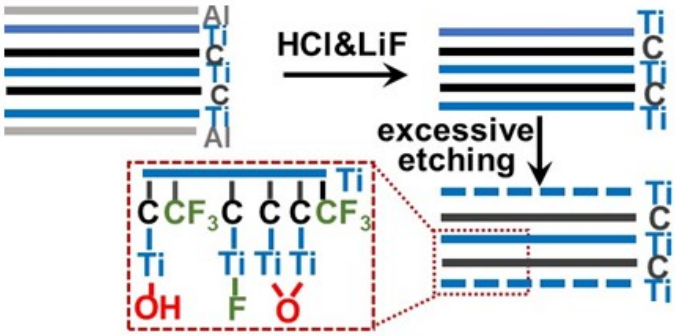


Figure S12. Schematic illustrations in the formation of $-CF_3$ terminations.

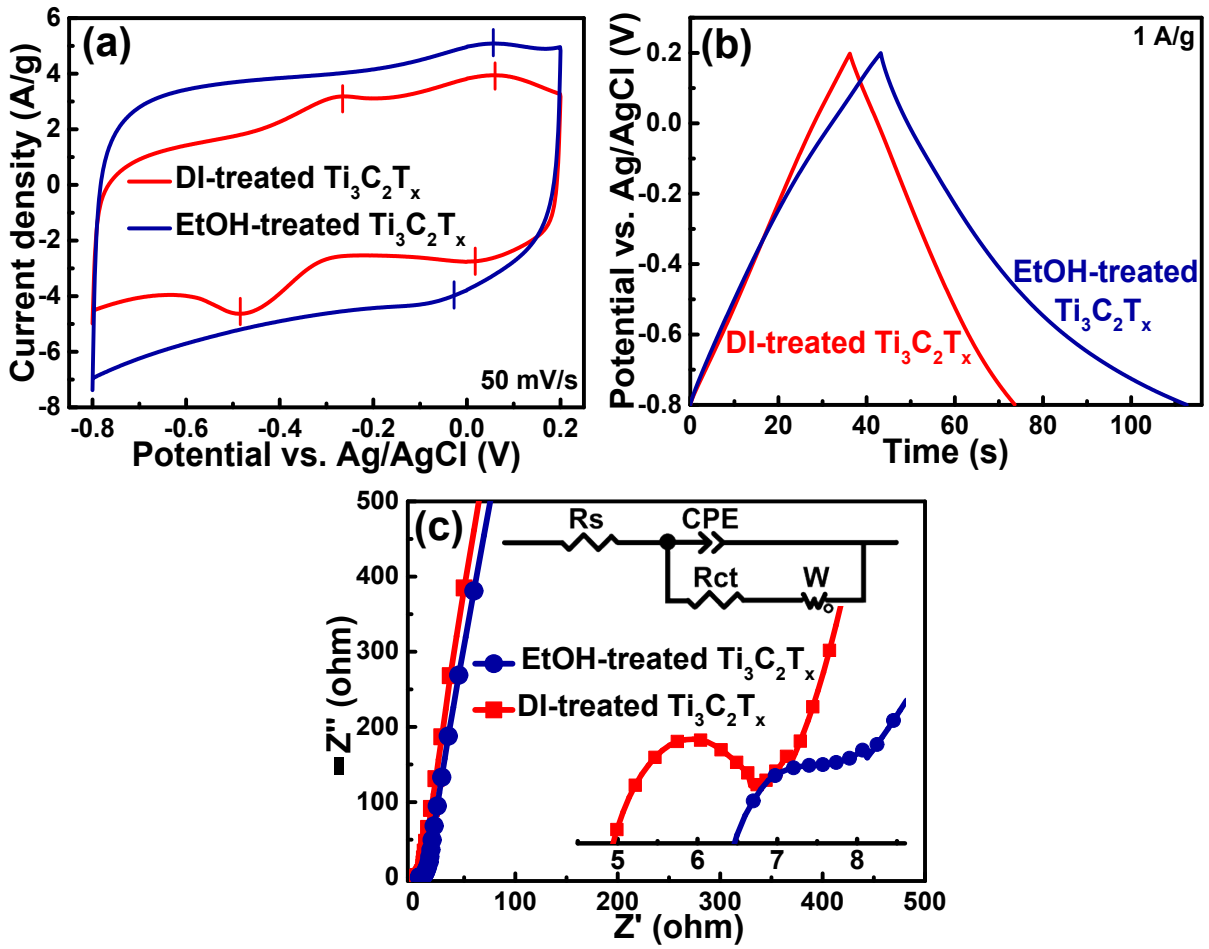


Figure S13. Electrochemical behaviors of DI- and EtOH-treated $Ti_3C_2T_x$ in 2 M aqueous KCl electrolytes. (a) CV curves at 50 mV $s^{-1}$ with a potential range of –0.8 to 0.2 V. (b) GCD curves at 1 A $g^{-1}$. (c) Electrochemical impedance spectroscopy with the equivalent circuit including solution resistance (Rs), charge-transfer (Rct) resistance, and Warburg impedance (W).

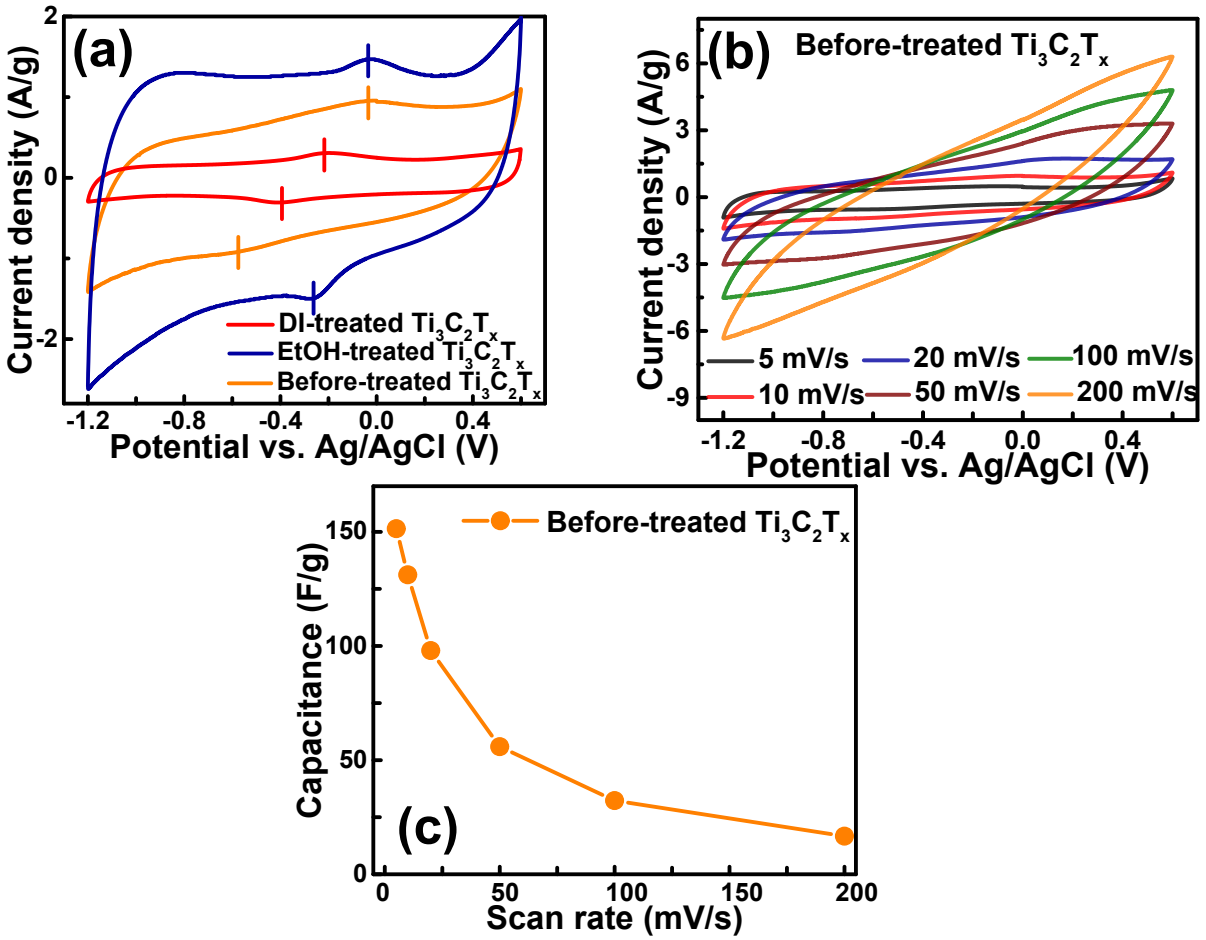


Figure S14. In 1 M EMITFSI ionic liquid electrolytes, electrochemical behaviors of solvent-free treated, DI-treated, and EtOH-treated $Ti_3C_2T_x$. (a) CV curves at 10 mV $s^{-1}$ with a potential range of –1.2 to 0.6 V. (b-c) CV curves and (c) rate performance of solvent-free treated $Ti_3C_2T_x$ at 5 to 200 mV $s^{-1}$.

Considerably different from the pair of redox peaks at –0.11 and –0.45 V in DI-treated $Ti_3C_2T_x$ (Figure S14a), the solvent-free and EtOH-treated $Ti_3C_2T_x$ revealed similar redox peaks at –0.02 V, indicating the preserved $–CF_3$-terminations in EtOH treatment when the formation during solvent-free treatments. Moreover, compared with DI-treated $Ti_3C_2T_x$ electrode (Figure S14b-c), solvent-free and EtOH-treated $Ti_3C_2T_x$ electrode showed better

specific capacitance and rate performance owing to structural properties as demonstrated in our current study.

Therefore, according to Figure S13, Figure S14, and Figure 3a, we can propose that the redox species of EtOH-treated $Ti_3C_2T_x$ might be $–CF_3$-related redox reactions, whereas those of DI-treated-$Ti_3C_2T_x$ might be $EMI^+$ cation intercalation/de-tercalations. The proposal was mainly based on the following reasons. (1) Highly consistent with the previous study[18] showing redox peaks at –0.2 V/–0.4 V in the EMIFTSI electrolyte, the DI-treated $Ti_3C_2T_x$ in current study displayed those at –0.28 V/–0.49 V and –0.11 V/–0.45 V in EMITFSI and KCl electrolytes, respectively, indicating $EMI^+$ cation intercalation/de-intercalation. (2) In the KCl electrolytes, our previous study[10] demonstrated 0.14 V/–0.04 V redox peaks in the –OH-terminated $Ti_3C_2T_x$, similar with the 0.05 V/–0.07 V redox peaks in $–CF_3$–terminated EtOH-treated $Ti_3C_2T_x$ owing to $–CF_3$ replacement by aqueous KCl solution, implying $K^+$ cation interaction/de-intercalation. (3) Whereas, compared with reason (1) and (2), the $–CF_3$–terminated EtOH-treated $Ti_3C_2T_x$ exhibits considerable differentiated redox peaks at –0.02 V/–0.29 V in EMITFSI electrolytes, demonstrating $–CF_3$-related redox reactions in the $Ti_3C_2T_x$.

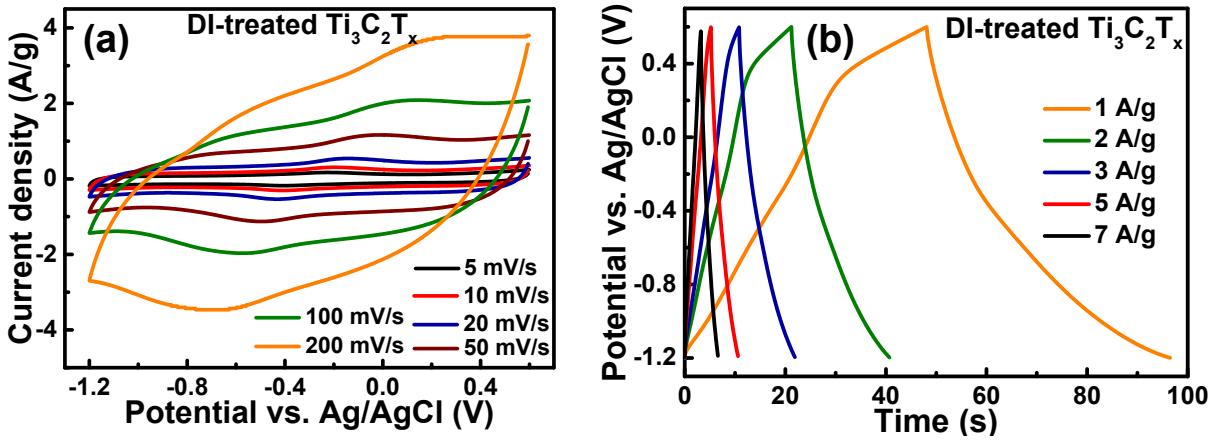


Figure S15. In 1 M EMITFSI ionic liquid electrolytes, (a) CV and (b) GCD curves of DI-treated $Ti_3C_2T_x$ at different scan rates of 5 to 200 mV $s^{-1}$ and current density of 1 to 7 A $g^{-1}$, respectively.

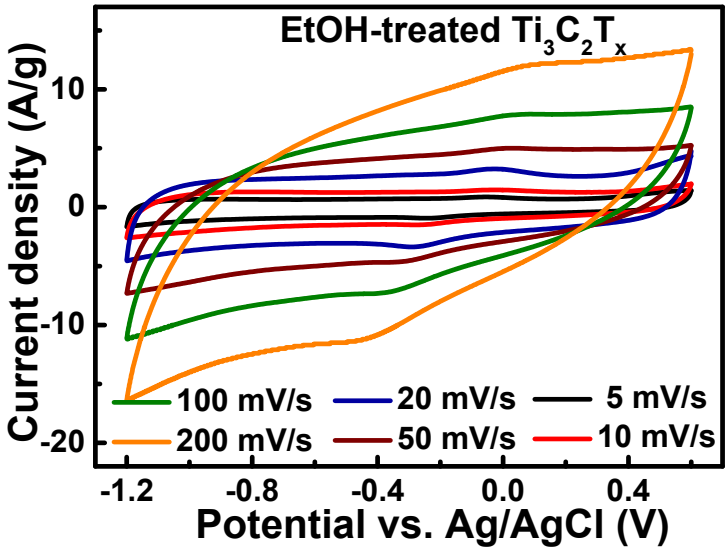


Figure S16. In 1 M EMITFSI ionic liquid electrolytes, CV curves of EtOH-treated $Ti_3C_2T_x$ at different scan rates of 5 to 200 mV $s^{-1}$.

**Table S4** Previously reported electrochemical performance of $Ti_3C_2T_x$ under various potential windows in ionic liquid electrolyte

| $Ti_3C_2T_x$ description | Electrolyte | Potential window [V] | Specific capacitance [F/g] at current density [mV/s] | Ref. |
|---|---|---|---|---|
| $Ti_3C_2T_x$ (–OH) | 1 M EMITFSI | 0~3 | 70 F/g (20 mV/s) | [19] |
| IL-$Ti_3C_2T_x$ | 1 M EMITFSI | –1.5~1.5 | 84 F/g (20 mV/s) | [20] |
| CNT/$Ti_3C_2T_x$ | 1 M EMITFSI/ACN | –0.8~1.0 | 85 F/g (2 mV/s) | [18] |
| $Ti_3C_2T_x$/TEAPW12 | 1 M $TEABF_4$/ACN | –2.2~0 | 36 F/g (1 mV/s) | [21] |
| PPy-$Ti_3C_2T_x$-IL | [EMIm][$NTf_2$] | 0~3 | 51.85 F/g (20 mV/s) | [22] |
| $Ti_3C_2T_x$-C12 | 1 M EMITFSI/ACN | –1.8~1 | 185 F/g (1 mV/s) | [23] |
| $Ti_3C_2T_x$-$MnFe_2O_4$ | 1 M $EMIMBF_4$ | –1.5~0.5 | 172 F/g (50 mV/s) | [24] |
| $Ti_3C_2T_x$-knotted CNT | 1 M EMITFSI/LiTFSI/ACN | –1.5~0.3 | 130 F/g (10 mV/s) | [25] |
| rGO | 0.5 M $BMIMBF_4$ | 0~2.5 | 135 F/g (5 mV/s) | [26] |
| –$CF_3$ terminated $Ti_3C_2T_x$ | 1 M EMITFSI/ACN | –1.2~0.6 | 295.3 F/g (5 mV/s) | Current Study |

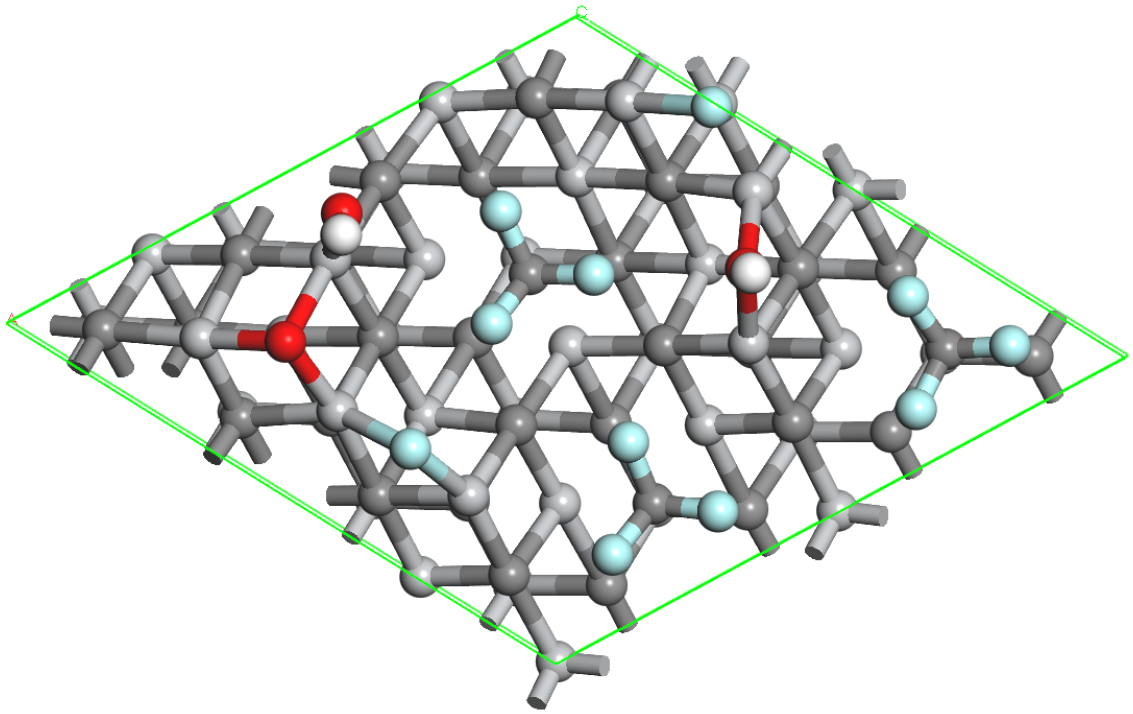

Figure S17. DFT calculated optimized structure of $Ti_3C_2T_x$.

**REFERENCES**


1. Kresse, G.; Furthmüller, J., Efficient iterative schemes for ab initio total-energy calculations using a plane-wave basis set. *Physical Review B* **1996,** *54* (16), 11169-11186.

2. Rappe, A. K.; Casewit, C. J.; Colwell, K. S.; Goddard, W. A.; Skiff, W. M., UFF, a full periodic table force field for molecular mechanics and molecular dynamics simulations. *Journal of the American Chemical Society* **1992,** *114* (25), 10024-10035.

3. Ding, L.; Wei, Y.; Li, L.; Zhang, T.; Wang, H.; Xue, J.; Ding, L.-X.; Wang, S.; Caro, J.; Gogotsi, Y., MXene molecular sieving membranes for highly efficient gas separation. *Nature Communications* **2018,** *9* (1), 155.

4. D.A. Case, I.Y. Ben-Shalom, S.R. Brozell, D.S. Cerutti, T.E. Cheatham, III, V.W.D. Cruzeiro, T.A. Darden, R.E. Duke, D. Ghoreishi, M.K. Gilson, H. Gohlke, A.W. Goetz, D.

Greene, R Harris, N. Homeyer, S. Izadi, A. Kovalenko, T. Kurtzman, T.S. Lee, S. LeGrand, P. Li, C. Lin, J. Liu, T. Luchko, R. Luo, D.J. Mermelstein, K.M. Merz, Y. Miao, G. Monard, C. Nguyen, H. Nguyen, I. Omelyan, A. Onufriev, F. Pan, R. Qi, D.R. Roe, A. Roitberg, C. Sagui, S. Schott-Verdugo, J. Shen, C.L. Simmerling, J. Smith, R. Salomon-Ferrer, J. Swails, R.C. Walker, J. Wang, H. Wei, R.M. Wolf, X. Wu, L. Xiao, D.M. York and P.A. Kollman (2018), AMBER 2018, University of California, San Francisco.

5. Gaussian 09, Revision D.01, M. J. Frisch, G. W. Trucks, H. B. Schlegel, G. E. Scuseria, M. A. Robb, J. R. Cheeseman, G. Scalmani, V. Barone, B. Mennucci, G. A. Petersson, H. Nakatsuji, M. Caricato, X. Li, H. P. Hratchian, A. F. Izmaylov, J. Bloino, G. Zheng, J. L. Sonnenberg, M. Hada, M. Ehara, K. Toyota, R. Fukuda, J. Hasegawa, M. Ishida, T. Nakajima, Y. Honda, O. Kitao, H. Nakai, T. Vreven, J. A. Montgomery, Jr., J. E. Peralta, F. Ogliaro, M. Bearpark, J. J. Heyd, E. Brothers, K. N. Kudin, V. N. Staroverov, R. Kobayashi, J. Normand, K. Raghavachari, A. Rendell, J. C. Burant, S. S. Iyengar, J. Tomasi, M. Cossi, N. Rega, J. M. Millam, M. Klene, J. E. Knox, J. B. Cross, V. Bakken, C. Adamo, J. Jaramillo, R. Gomperts, R. E. Stratmann, O. Yazyev, A. J. Austin, R. Cammi, C. Pomelli, J. W. Ochterski, R. L. Martin, K. Morokuma, V. G. Zakrzewski, G. A. Voth, P. Salvador, J. J. Dannenberg, S. Dapprich, A. D. Daniels, Ö. Farkas, J. B. Foresman, J. V. Ortiz, J. Cioslowski, and D. J. Fox, Gaussian, Inc., Wallingford CT, 2009.

6. Mashtalir, O.; Naguib, M.; Mochalin, V. N.; Dall'Agnese, Y.; Heon, M.; Barsoum, M. W.; Gogotsi, Y., Intercalation and delamination of layered carbides and carbonitrides. *Nature Communications* **2013,** *4* (1), 1716.

7. Han, M.; Yin, X.; Wu, H.; Hou, Z.; Song, C.; Li, X.; Zhang, L.; Cheng, L., $Ti_3C_2$ MXenes with Modified Surface for High-Performance Electromagnetic Absorption and Shielding in the X-Band. *ACS Applied Materials & Interfaces* **2016,** *8* (32), 21011-21019.

8. Halim, J.; Kota, S.; Lukatskaya, M. R.; Naguib, M.; Zhao, M.-Q.; Moon, E. J.; Pitock, J.; Nanda, J.; May, S. J.; Gogotsi, Y.; Barsoum, M. W., Synthesis and Characterization of 2D Molybdenum Carbide (MXene). *Advanced Functional Materials* **2016,** *26* (18), 3118-3127.

9. Ran, J.; Gao, G.; Li, F.-T.; Ma, T.-Y.; Du, A.; Qiao, S.-Z., Ti3C2 MXene co-catalyst on metal sulfide photo-absorbers for enhanced visible-light photocatalytic hydrogen production. *Nature Communications* **2017,** *8* (1), 13907.

10. Qian, A.; Seo, J. Y.; Shi, H.; Lee, J. Y.; Chung, C.-H., Surface Functional Groups and Electrochemical Behavior in Dimethyl Sulfoxide-Delaminated $Ti_3C_2T_x$ MXene. *ChemSusChem* **2018,** *11* (21), 3719-3723.

11. Rakhi, R. B.; Ahmed, B.; Hedhili, M. N.; Anjum, D. H.; Alshareef, H. N., Effect of Postetch Annealing Gas Composition on the Structural and Electrochemical Properties of $Ti_2CT_x$ MXene Electrodes for Supercapacitor Applications. *Chem. Mater.* **2015,** *27* (15), 5314-5323.

12. Shah, S. A.; Habib, T.; Gao, H.; Gao, P.; Sun, W.; Green, M. J.; Radovic, M., Template-free 3D titanium carbide ($Ti_3C_2T_x$) MXene particles crumpled by capillary forces. *Chemical Communications* **2017,** *53* (2), 400-403.

13. Zhao, J.; Zhang, L.; Xie, X.-Y.; Li, X.; Ma, Y.; Liu, Q.; Fang, W.-H.; Shi, X.; Cui, G.; Sun, X., $Ti_3C_2T_x$ (T= F, OH) MXene nanosheets: conductive 2D catalysts for ambient

electrohydrogenation of $N_2$ to $NH_3$. *Journal of Materials Chemistry A* **2018,** *6* (47), 24031-24035.

14. You, S. A.; Kwon, O. S.; Jang, J., A facile synthesis of uniform Ag nanoparticle decorated CVD-grown graphene via surface engineering. *Journal of Materials Chemistry* **2012,** *22* (34), 17805-17812.

15. Chen, W. Y.; Lai, S.-N.; Yen, C.-C.; Jiang, X.; Peroulis, D.; Stanciu, L. A., Surface Functionalization of $Ti_3C_2T_x$ MXene with Highly Reliable Superhydrophobic Protection for Volatile Organic Compounds Sensing. *ACS Nano* **2020,** *14* (9), 11490-11501.

16. Yazdanparast, S.; Soltanmohammad, S.; Fash-White, A.; Tucker, G. J.; Brennecka, G. L., Synthesis and Surface Chemistry of 2D TiVC Solid-Solution MXenes. *ACS Applied Materials & Interfaces* **2020,** *12* (17), 20129-20137.

17. Schultz, T.; Frey, N. C.; Hantanasirisakul, K.; Park, S.; May, S. J.; Shenoy, V. B.; Gogotsi, Y.; Koch, N., Surface Termination Dependent Work Function and Electronic Properties of $Ti_3C_2T_x$ MXene. *Chemistry of Materials* **2019,** *31* (17), 6590-6597.

18. Dall'Agnese, Y.; Rozier, P.; Taberna, P.-L.; Gogotsi, Y.; Simon, P., Capacitance of two-dimensional titanium carbide (MXene) and MXene/carbon nanotube composites in organic electrolytes. *J. Power Sources* **2016,** *306*, 510-515.

19. Lin, Z.; Barbara, D.; Taberna, P.-L.; Van Aken, K. L.; Anasori, B.; Gogotsi, Y.; Simon, P., Capacitance of $Ti_3C_2T_x$ MXene in ionic liquid electrolyte. *J. Power Sources* **2016,** *326*, 575-579.

20. Lin, Z.; Rozier, P.; Duployer, B.; Taberna, P.-L.; Anasori, B.; Gogotsi, Y.; Simon, P., Electrochemical and in-situ X-ray diffraction studies of $Ti_3C_2T_x$ MXene in ionic liquid electrolyte. *Electrochem. Commun.* **2016,** *72*, 50-53.

21. Zhu, J.-J.; Hemesh, A.; Biendicho, J. J.; Martinez-Soria, L.; Rueda-Garcia, D.; Morante, J. R.; Ballesteros, B.; Gomez-Romero, P., Rational design of MXene/activated carbon/polyoxometalate triple hybrid electrodes with enhanced capacitance for organic-electrolyte supercapacitors. *Journal of Colloid and Interface Science* **2022,** *623*, 947-961.

22. Fan, Q.; Zhao, R.; Yi, M.; Qi, P.; Chai, C.; Ying, H.; Hao, J., Ti3C2-MXene composite films functionalized with polypyrrole and ionic liquid-based microemulsion particles for supercapacitor applications. *Chemical Engineering Journal* **2022,** *428*, 131107.

23. Liang, K.; Matsumoto, R. A.; Zhao, W.; Osti, N. C.; Popov, I.; Thapaliya, B. P.; Fleischmann, S.; Misra, S.; Prenger, K.; Tyagi, M.; Mamontov, E.; Augustyn, V.; Unocic, R. R.; Sokolov, A. P.; Dai, S.; Cummings, P. T.; Naguib, M., Engineering the Interlayer Spacing by Pre-Intercalation for High Performance Supercapacitor MXene Electrodes in Room Temperature Ionic Liquid. *Adv. Funct. Mater.* **2021,** *31* (33), 2104007.

24. Shi, M.; Narayanasamy, M.; Yang, C.; Zhao, L.; Jiang, J.; Angaiah, S.; Yan, C., 3D interpenetrating assembly of partially oxidized MXene confined Mn–Fe bimetallic oxide for superior energy storage in ionic liquid. *Electrochimi. Acta* **2020,** *334*, 135546.

25. Gao, X.; Du, X.; Mathis, T. S.; Zhang, M.; Wang, X.; Shui, J.; Gogotsi, Y.; Xu, M., Maximizing ion accessibility in MXene-knotted carbon nanotube composite electrodes for high-rate electrochemical energy storage. *Nat. Commun.* **2020,** *11* (1), 6160.

26. Mourad, E.; Coustan, L.; Lannelongue, P.; Zigah, D.; Mehdi, A.; Vioux, A.; Freunberger, Stefan A.; Favier, F.; Fontaine, O., Biredox ionic liquids with solid-like redox density in the liquid state for high-energy supercapacitors. *Nat. Mater.* **2017,** *16* (4), 446-453.